UC Irvine
UC Irvine Previously Published Works

Title
Self-Deposition of 2D Molybdenum Sulfides on Liquid Metals

Permalink

Journal

ISSN

Authors
Wang, Yifang
Mayyas, Mohannad
Yang, Jiong
et al.

Publication Date

DOI

Copyright Information

Peer reviewed

Self-Deposition of 2D Molybdenum Sulfides on Liquid Metals

Yifang Wang, Mohannad Mayyas,* Jiong Yang, Jianbo Tang, Mohammad B. Ghasemian, Jialuo Han, Aaron Elbourne, Torben Daeneke, Richard B. Kaner, and Kourosh Kalantar-Zadeh*

2D transition metal dichalcogenides (TMDs) play increasingly significant roles in research and future optoelectronics. However, the large-scale deposition of 2D TMDs remains challenging due to sparse nucleation and substrate dependency. Liquid metals can offer effective solutions to meet these challenges due to their reactive, non-polarized, and templating properties. Here, self-deposition of 2D molybdenum sulfide is shown by introducing a molybdenum precursor onto the surface of a eutectic alloy of gallium and indium (EGaIn). EGaIn serves as an ultra-smooth template and reducing agent for the precursor to form large-scale planar molybdenum sulfides, which is transferrable to any substrate. The molybdenum sulfides form spontaneously on the surface of EGaIn, which has a sufficient potential to drive the cathodic reactions of the deposition process. A highly crystalline $2H\text{-}MoS_2$ is obtained after a final annealing step. This work demonstrates a fundamentally new capability for the formation of large-scale 2D TMDs.

1. Introduction

Several high entropy gallium-based metal alloys offer low melting points at near room temperature. The most well-known examples are eutectic alloy of gallium and indium (EGaIn) and galinstan (eutectic alloys of gallium, indium, and tin) with melting points at 15.4 and 13.2 °C, respectively.[1] Such alloys are commonly referred to as liquid metals since they take on a liquid state at room temperature. They are fascinating liquid metal alloys as they offer fluidity, freely moving electrons and ions, as well as metallic thermal and electrical conductivity.[2] Additionally, gallium (Ga) is not as hazardous as its sister liquid metal mercury.[2c,3] Other than these unique properties, liquid metals also extend intrinsic characteristics that render them unique as reaction media for synthesizing 2D materials.[4] One of the key properties is that the surface of liquid metal is atomically smooth which can naturally template 2D materials. Another advantage of liquid metals is their non-polarized nature,[4a] which makes the attractive forces between the bulk metal and the interfacial 2D materials weak.[4a] Consequently, the synthesized 2D material can be readily harvested with a mechanical delamination process.[4]

We have previously shown that liquid metals can be used for synthesizing self-limiting oxide or sulfide metal compounds on their surface directly from the mother melt by exposing them to oxic or sulfuric gaseous environments.[4a,5] Another possibility involves adding a secondary metallic element into the liquid metal to make an alloy.[4a] If the secondary metal wins the competition against the core metal,[4a] it emerges on the surface and its oxide or sulfide can be harvested. However, this gaseous-surrounding-based process only works if the secondary metal is soluble in the host liquid metal. This means that metallic elements such as tungsten (W) and molybdenum (Mo), which are not soluble in Ga, cannot be obtained using this method.[1] We hypothesize that in this case, by bringing a precursor of these metals to the surface of liquid metal, a designed reaction can take place to form the desired 2D compound.

By the careful selection of liquid metals and precursors in their surroundings, unique reactive interfacial environments can be created. These precursors can be dissolved in a solvent

Y. Wang, Dr. M. Mayyas, Dr. J. Yang, Dr. J. Tang, Dr. M. B. Ghasemian, J. Han, Prof. K. Kalantar-Zadeh
School of Chemical Engineering
University of New South Wales (UNSW)
Sydney Campus, Sydney, New South Wales 2052, Australia
E-mail: m.mayyas@unsw.edu.au; k.kalantar-zadeh@unsw.edu.au

Dr. A. Elbourne
School of Science
RMIT University
Melbourne, Victoria 3001, Australia

Dr. T. Daeneke
School of Engineering
RMIT University
Melbourne, Victoria 3001, Australia

Prof. R. B. Kaner
Department of Chemistry and Biochemistry and
California NanoSystems Institute
University of California Los Angeles (UCLA)
Los Angeles, CA 90095, USA

Prof. R. B. Kaner
Department of Materials Science and Engineering and
California NanoSystems Institute
University of California Los Angeles (UCLA)
Los Angeles, CA 90095, USA

to be brought onto this interface. The interfacial region between the liquid metal and solvent can be destabilized to activate the precursors and produce the target material, while the atomically smooth liquid metal surface serves as a template to promote ultra-smooth crystalline planes. Utilizing this route, we have previously demonstrated the creation of 2D graphitic films on the surface of liquid metals via electrochemical processes.[6] Here Mayyas et al. utilized various organic solvents as the carbon sources, and ultra-thin carbon films were deposited onto the surface of liquid metals upon applying external potentials. However, avoiding an electrochemical process is advantageous, as it limits the applied energy to confine the interfacial growth into mono or several layers.

In this work, we show the formation of 2H-molybdenum disulfide (MoS_2), which is a popular member of the 2D materials family,[7] using the liquid metal alloy, EGaIn, with an interfacial process. A consecutive set of reactions and washing steps are carried out, using a molybdenum precursor, to induce the self-deposition of ultra-thin molybdenum sulfide on the surface of EGaIn. A liquid metal's surface exhibits a negative surface charge in an acidic environment.[8] When the reactive species of the molybdenum sulfide precursor are introduced onto the surface of EGaIn, they undergo a self-deposition process to produce 2D molybdenum sulfide.

2. Results and Discussion

In brief, prior to deposition, hydrochloric acid (HCl) was used to wash the EGaIn droplet thereby removing the gallium oxide layer and inducing intimate contact between the EGaIn and solvent for creating a reactive interfacial environment. After washing with HCl, an aqueous solution of ammonium tetrathiomolybdate ($(NH_4)_2MoS_4$) was applied. Immediately, a uniform layer of molybdenum sulfide formed on the interface, and subsequently the surface was washed to hinder any further growth. A detailed description of the synthesis process can be found in the Supporting Information.

The mechanism by which the molybdenum sulfide (MoS_x) self-deposits on the surface of EGaIn is schematically illustrated
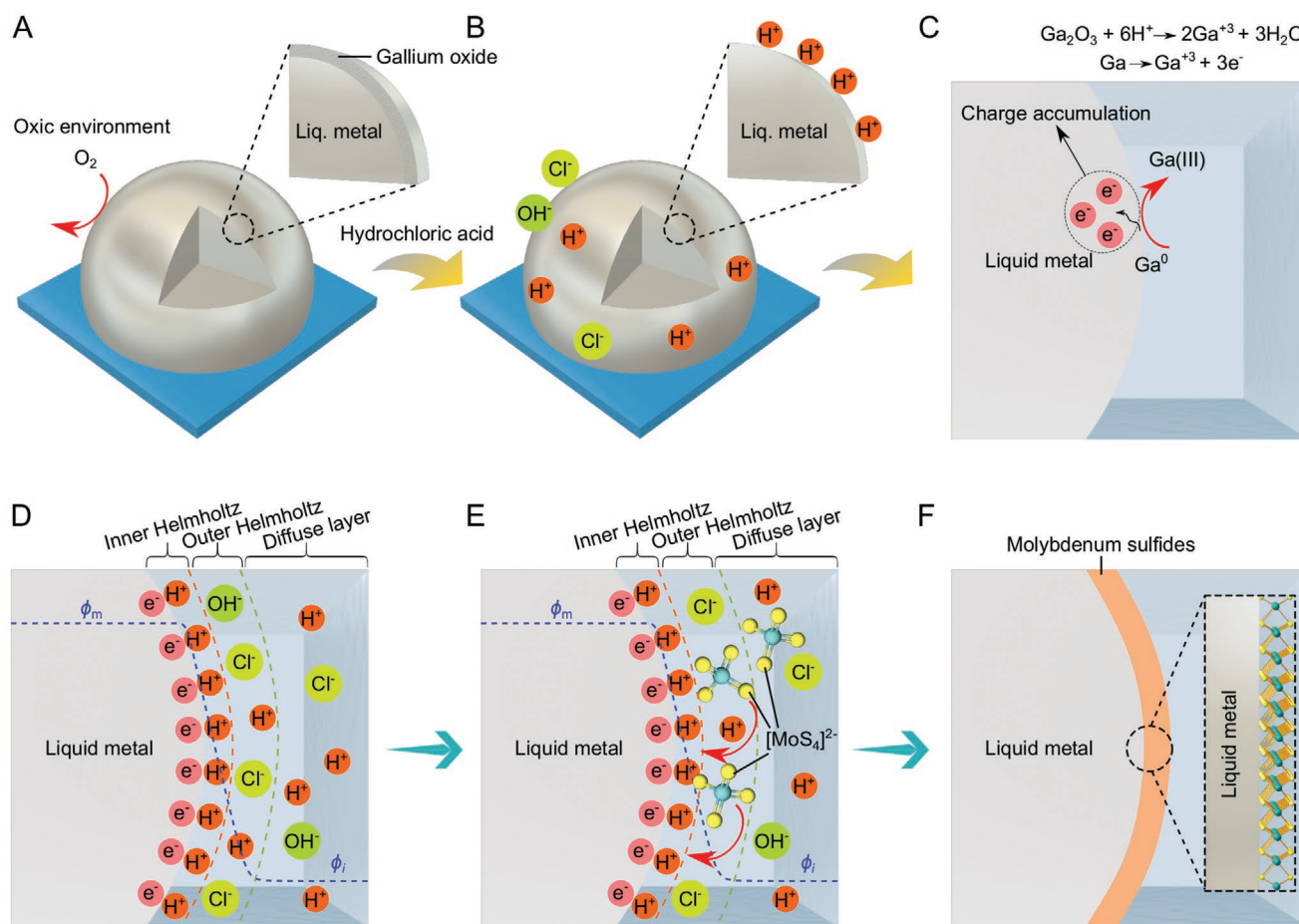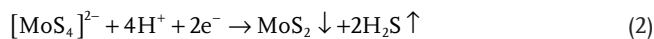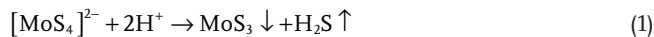

Figure 1. Schematic illustration of MoS_x formation on EGaIn. A) The formation of a gallium oxide passivating layer on the surface of liquid metal under an oxic environment. B) The removal of the oxide interfacial layer. C) The build-up of surface charge on the liquid metal. Here electrons saturate the liquid metal surface and system equilibrium is reached. D) Electron confinement and the Helmholtz layer formation on the surface of liquid metal. The blue line is a hypothetical representation of the interfacial potential (potential drop = $\Phi_m - \Phi_i$). E) Anionic substitution by $[MoS_4]^{2-}$ in the outer Helmholtz layer and subsequent reaction with the H^+ in the inner Helmholtz layer. F) The formation of an ultra-smooth interfacial film of 2D molybdenum sulfides.

in **Figure 1**. It has been established that when exposed to an oxic environment, Ga-based liquid metals form a passivating oxide layer of gallium on their surface (Figure 1A) as gallium oxide has a lower Gibb's free energy than that of indium oxide.[4a] For removing the oxide surface layer and exposing the surface of the liquid metal, the droplet was washed with HCl (Figure 1B). EGaIn as a metal offers excessive electrons on its surface and this attracts the H^+ ions after washing (Figure 1C). The surface of the EGaIn becomes saturated with electrons and reaches an equilibrium, where no oxidation occurs at the interface between the liquid metal and the acidic aqueous solution. This phenomenon is known to induce a surface potential on metals (Φ_m). The surface potential of EGaIn is neutralized by counter-ions creating what is commonly referred to as the electrical double-layer (EDL).[9] Figure 1D features the different zones of the EDL. In the inner Helmholtz layer, the H^+ counter ions adhere directly to the surface of the EGaIn droplet. The interfacial potential remains unbalanced in this region, and a combination of co-ions and counter-ions is established in the outer Helmholtz layer to reach the equilibrium potential (Φ_i).[10] When $(NH_4)_2MoS_4$ is added onto the EGaIn droplet, the anions in the outer Helmholtz layer are substituted by the $[MoS_4]^{2-}$ (Figure 1E). These ions, in turn, react with the H^+ in the inner Helmholtz layer according to Equation (1)[11] forming MoS_3. Further reduction can occur in the inner Helmholtz layer by the interfacial potential of Φ_m according to Equation (2) to form MoS_2. The interfacial product is collectively described here as MoS_x. Weak interfacial forces hold the interfacial MoS_x film on the EGaIn surface as featured in Figure 1F. The EGaIn droplet provides both the interfacial potential to destabilize the $[MoS_4]^{2-}$ and serves as an atomically flat template, yielding a smooth and uniform 2D MoS_x.

$$[MoS_4]^{2-} + 2H^+ \rightarrow MoS_3 \downarrow + H_2S \uparrow \tag{1}$$

$$[MoS_4]^{2-} + 4H^+ + 2e^- \rightarrow MoS_2 \downarrow + 2H_2S \uparrow \tag{2}$$

To further elucidate the mechanism by which MoS_x deposits onto the EGaIn surface, electrochemical assessment was employed. The electrochemical stability of the $(NH_4)_2MoS_4$ aqueous system was explored using a three-electrode system with a gold working electrode at different scan rates as presented in **Figure 2**A (details provided in the Supporting Information). The anodic region, at a potential more positive than −0.50 V, corresponds to the deposition of sulfur saturated MoS_3 (Equation (3)). In the potential range from −0.56 to −1.3 V, a cathodic region is observed, corresponding to both $[MoS_4]^{2-}$ deposition onto the gold electrode (Equation (2)) and reduction of the MoS_3 (Equation (4)).[12] The onset voltage for the reduction of $[MoS_4]^{2-}$ was determined to be −0.56 V. The chemically deposited material during cyclic voltammetry measurements was confirmed to be MoS_x by scanning electron microscopy
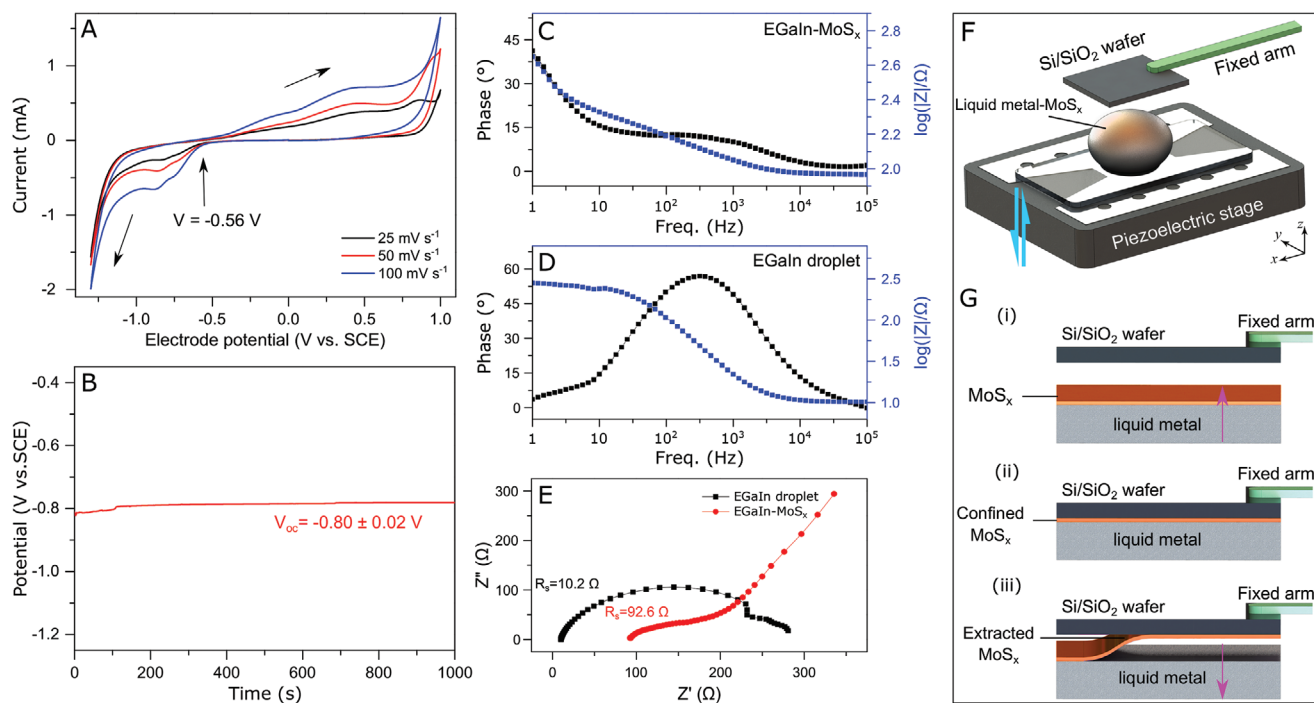

Figure 2. Electrochemical characterization of the $((NH_4)_2MoS_4)$ aqueous system and schematic illustrations for the extraction of the MoS_x layer. A) Cyclic voltammetry profiles of $((NH_4)_2MoS_4)$ aqueous solution acquired at different scan rates, scanned in the potential window from 1.0 to −1.3 V (negative scan), initial and final voltages were both set to 0.0 V versus SCE. B) The open-circuit voltage (V_{oc}) measurement of the EGaIn droplet in an aqueous solution versus time over 1000 s. C,D) A Bode plot of the EGaIn droplet with and without the MoS_x interfacial layer; scan conditions: 1.92 mM $(NH_4)_2MoS_4$ and 0.10 M KCl as the electrolyte, −0.50 V. E) A Nyquist plot of an EGaIn droplet with and without the MoS_x interfacial layer, the recorded values of series resistance (R_s) are 10.2 and 92.6 Ω, respectively; scan conditions: 1.92 mM $(NH_4)_2MoS_4$ and 0.10 M KCl as the electrolyte, −0.50 V. F) Schematics of the experimental set up for the extraction of a MoS_x layer from the EGaIn surface. G) A cross-sectional schematic illustration of the extracting and transferring processes.

(SEM) and energy dispersive X-ray (EDX) mapping (Figure S1, Supporting Information), X-ray photoelectron spectroscopy (XPS) (Figure S2, Supporting Information) and Raman spectroscopy (Figure S3, Supporting Information). As can be seen, the surface of the electrodeposited film onto gold is quite rough signifying the importance of using the atomically smooth surface of EGaIn for avoiding such nucleation formation.

$$[MoS_4]^{2-} \rightarrow MoS_3 \downarrow + 1/8 S_8 + 2e^- \qquad (3)$$

$$MoS_3 + 1/8 S_8 + 2e^- \rightarrow [MoS_4]^{2-} \qquad (4)$$
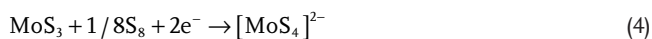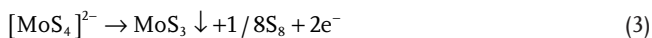
In the second set of electrochemical experiments, the working electrode was replaced with EGaIn in order to assess the open-circuit voltage (V_{oc}) of a fresh EGaIn droplet, corresponding to the interfacial potential. This experiment was conducted to determine whether the V_{oc} is sufficient to destabilize $[MoS_4]^{2-}$ at the interface of EGaIn. As a reference, the V_{oc} was acquired in an aqueous solution without $[MoS_4]^{2-}$ ions, with the same pH as the initial precursor solution, over 1000 s as presented in Figure 2B. This V_{oc} is ≈-0.80 V versus saturated calomel electrode (SCE). This value is considerably more negative than the onset potential of $[MoS_4]^{2-}$ reduction (–0.56 V, as determined on a gold electrode), suggesting that the charge accumulation and the interfacial potential between the interface of EGaIn and the aqueous solution is sufficient to reduce the $[MoS_4]^{2-}$ species into a MoS$_x$ layer.

To initially confirm that the produced MoS$_x$ layer on EGaIn was present and of high integrity, potentiostatic electrochemical impedance spectroscopy (EIS) was performed on the droplet with and without the self-deposited MoS$_x$ layer. The presence of a uniform interfacial semiconducting MoS$_x$ layer on the metal surface induces changes in the impedance of the electrochemical system. As shown in Figure 2C,D, the impedance was higher for the EGaIn-MoS$_x$ than EGaIn only, at all frequencies. A capacitive double layer appears to develop on the EGaIn droplet at frequencies of >10 Hz. This capacitive component is not present in the EGaIn-MoS$_x$ due to the interfacial layer reducing the charge transfer and thus the formation of a double-layer capacitance. Only at frequencies of <10 Hz, the EGaIn-MoS$_x$ shows a capacitive component due to the transpassive effect. The drop in the capacitive component of an EGaIn droplet at a frequency of <10 Hz can be attributed to the rapid formation of the EDL and its saturation creating an electric barrier on the surface.

The Nyquist plots, Figure 2E, feature a higher series resistance (R_s) for EGaIn-MoS$_x$ (92.6 Ω) compared to that of the EGaIn droplet (10.2 Ω), further suggesting that the MoS$_x$ layer on EGaIn is uniform and without any pores.[13] The optical images of both the electrodeposited MoS$_x$ on gold and self-deposited MoS$_x$ on EGaIn are presented in Figure S3, Supporting Information, and the AFM images in Figure S4, Supporting Information. The self-deposited MoS$_x$ shows a smooth and uniform surface with a roughness average (R_a) of 0.261 nm while the one electrodeposited onto solid gold electrode exhibits a porous and rough morphology with a R_a of 9.51 nm. This provides further evidence for the templating advantage of EGaIn's smooth interface. Additionally, from the electrochemical assessments, it was seen that the intrinsic EDL of EGaIn can be utilized for depositing MoS$_x$, without applying any external stimulant.

To achieve the accurate exfoliation and transfer of the self-deposited MoS$_x$ layers from the EGaIn surface onto a desired substrate, a program-controlled piezo-electric stage (touch-printing process) was utilized (see Methods section in Supporting Information for details). This program-controlled stage of 0.5 nm spatial steps are utilized to carry out the touch-printing process. The high-resolution stage allows the transfer of large-area layers (as large as several mm—Figure S5, Supporting Information) and increases the stability and reproducibility of the process. The transfer was conducted onto a variety of substrates including Si/SiO$_2$ (285 nm) and sapphire wafers (Figures S5 and S6, Supporting Information). The transfer process is schematically illustrated in Figure 2F. Further details on the synthesis and transfer of MoS$_x$ are provided in the Methods section in Supporting Information. Due to the non-polar nature of EGaIn, interactions between the metal and the synthesized 2D materials on its surface is weak.[13a] Conversely, the forces between MoS$_x$ and oxygen terminated substrates (such as SiO$_2$ and sapphire) are stronger due to the van der Waals forces between the permanent dipoles.[14] As such, this transferring technique can be applied to any polar substrate with O−, OH− or S− termination. When the substrate is brought into contact with the EGaIn, the 2D layer on its surface adheres to the substrate and separates itself from the parent liquid metal. Residual liquid metal inclusions are sometimes found on the transferred 2D layers that can be removed by an ultrasonic bath in ethanol.

After being transferred onto the substrate, the material appears to be a uniform sheet with a thickness of $\approx$1 nm as determined by atomic force microscopy (AFM) imaging (Figure S4A, Supporting Information). The XPS analysis confirmed that this sheet was MoS$_x$. The high-resolution XPS spectra at the Mo3d and S2p regions are shown in Figure S7A,B, Supporting Information. In the high-resolution XPS spectra of the S2p region, one doublet at 162 and 163.3 eV is observed, which corresponds to S^{2-} from molybdenum sulfide.[15] In the Mo3d region, the peaks are fit to two doublets, representing two chemical states of Mo and one single peak of S2s at 226.2 eV. The doublet at 230.0 and 233.3 eV can be attributed to Mo^{4+} 3d$_{5/2}$ and Mo^{4+} 3d$_{3/2}$ peaks, respectively. The doublet with higher binding energies of 232.8 and 235.9 eV belongs to Mo^{6+} from MoO$_3$, while the doublet at 230.0 and 233.3 eV belongs to Mo^{4+} from molybdenum sulfide.[15] Based on elemental analysis, the stoichiometric ratio of Mo^{4+} to S in molybdenum sulfide is 1.82:1, indicating the presence of substantial S-vacancies in the synthesized material. The XPS peaks are slightly broader than that of single-crystal MoS$_2$, which can be attributed to the presence of convoluted peaks from multiple oxidation states of the material.[16] Overall, the product of the self-deposition process is identified as S-deficient MoS$_x$ with MoO$_3$ inclusions.

A transmission electron microscopy (TEM) image and a selected area electron diffraction (SAED) pattern of a sample MoS$_x$ sheet are shown in Figure S8B,C, Supporting Information. The translucent appearance of the sheet in the TEM image suggests its thin nature in confirmation to AFM measurements, and the absence of any diffraction dots or rings in the SAED pattern suggests low crystallinity of the product. Therefore, an annealing process was applied to obtain stoichiometric and crystalline 2D MoS$_2$ sheets. Annealing was conducted in multiple steps as described in the Supporting Information.
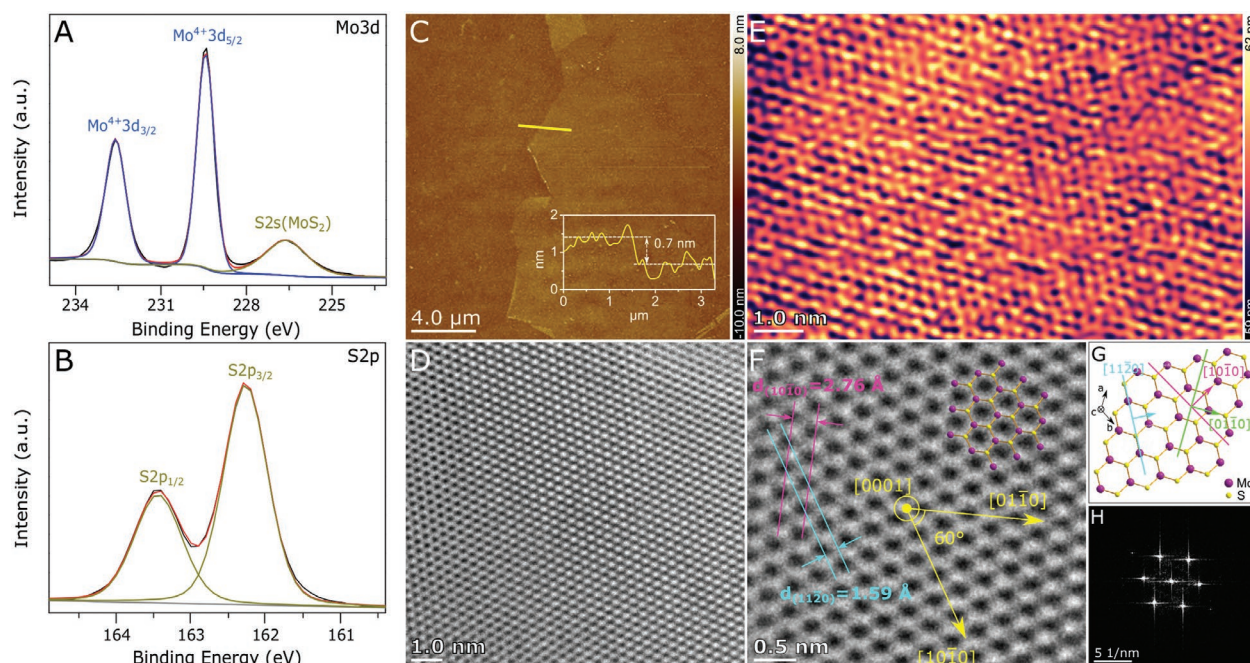
**ADVANCED
SCIENCE NEWS**
www.advancedsciencenews.com

**ADVANCED
FUNCTIONAL
MATERIALS**
www.afm-journal.de

Figure 3. The high-resolution XPS of the crystalline MoS$_2$ sheets at A) Mo3d and B) S2p region. AFM and TEM characterizations of the 2D MoS$_2$. C) AFM image with the inset representing the thickness of ≈0.7 nm. E) High-resolution AFM image. D,F) HR-TEM image. G) The representation of the crystal structure. H) The fast Fourier transform (FFT) pattern.

Characteristic Raman peaks of MoS$_2$ show up after annealing (the full range of Raman spectra for the layers after each step are shown Figure S9, Supporting Information).

Figure 3A,B show the XPS of the sheets, after annealing, at Mo3d and S2p regions. The doublet in the Mo3d region corresponds to the 3d$_{5/2}$ and 2d$_{3/2}$ orbital of Mo^{6+}, and the single peak is attributed to the *2s* peak of divalent sulfide ions (S^{2-}). The doublet in the S2p region corresponds to the 2p$_{1/2}$ and 2p$_{3/2}$ orbital of S^{2-}. The ratio of Mo^{4+} to S is 1: 2.03. As such, the XPS results confirm the product to be MoS$_2$ sheets.[16] AFM image (Figure 3C) shows a smooth and uniform sheet. A line scan across the edge of the sheet presents a reduced step height of ≈0.7 nm after annealing, which is in line with the reported thickness of MoS$_2$ monolayers.[17] Atomic resolution AFM imaging (Figure 3E) presents a repeated hexagonal pattern, which indicates a high crystallinity of the resultant sheets. In order to gain further insight into the atomic structure of the synthesized nanosheets, high-resolution TEM (HR-TEM) was conducted as presented in Figure 3D,F (presented at different resolutions). A thermally robust silicon nitride (Si$_3$N$_4$) grid was utilized here since the copper grid with lacy carbon could not sustain the high-temperature annealing process. The HR-TEM image clearly reveals a honeycomb atomic arrangement with 2H-MoS$_2$. The d-spacing of [10$\overline{1}$0] plane is 2.76 Å, and the d-spacing of [11$\overline{2}$0] plane is 1.59 Å, which is in agreement with the reported structure of 2H-MoS$_2$ crystal,[12b] as is shown in Figure 3G. The fast Fourier transform pattern (Figure 3H) displays perfect hexagonal symmetrical patterns, indicating the hexagonal lattice structure of MoS$_2$ crystals. The TEM image of the folded edge of the MoS$_2$ layer is presented in Figure S10, Supporting Information. The spacing between layers is ≈0.66 nm, which is in agreement with the thickness

of monolayer MoS$_2$.[12b] A large area HR-TEM image of the 2D MoS$_2$ (Figure S11, Supporting Information) shows a single crystalline material with no observed grain boundaries.

Raman spectra and photoluminescence (PL) characterization of the 2D-MoS$_2$ sheets of different thicknesses were collected and presented in **Figure 4**. An optical microscopy image of a sample with different thicknesses is presented in Figure 4A. It has been established that for few-layer MoS$_2$ the frequency difference between the E^1_{2g} and A_{1g} mode can be used for determining the number of layers.[18] As shown in Figure 4B, Raman spectra of 2D-MoS$_2$ present characteristic E^1_{2g} and A_{1g} modes, which correspond to the in-plane optical vibrations of the Mo and S atoms and the out-of-plane optical vibrations of the S atoms, respectively. With the number of layers increasing from 1 layer to 5, the E^1_{2g} mode goes through a redshift from 388.1 to 385.3 cm^{-1} and the A_{1g} mode goes through a blueshift from 408.2 to 409.6 cm^{-1} (Figure 4C). The difference between the A_{1g} and E^1_{2g} modes increased from 20.1 cm^{-1} for the monolayer 2H-MoS$_2$ to 24.2 cm^{-1} for multi-layer 2H-MoS$_2$ (Figure 4D), which is in agreement with the reported value of chemical vapor deposited MoS$_2$[19] and indicates the highly crystalline quality of the resultant 2D sheets. PL spectra of 2H-MoS$_2$ have been reported to also be a function of MoS$_2$ thickness.[20] As shown in Figure 4E, the PL of monolayer MoS$_2$ presents two excitation peaks at 620 and 656 nm, which correspond to the B and A excitations modes of MoS$_2$.[21] As the thickness increases, both PL peaks go through slight blueshifts and these PL shifts agree well with past observations[21] and further proved the ability of the liquid metal process in obtaining high-quality 2H-MoS$_2$ from one to several layers.

In order to further characterize the resultant 2H-MoS$_2$ surface homogeneity at a large scale, Raman mapping was carried out. An example is presented in **Figure 5**. The optical microscopy
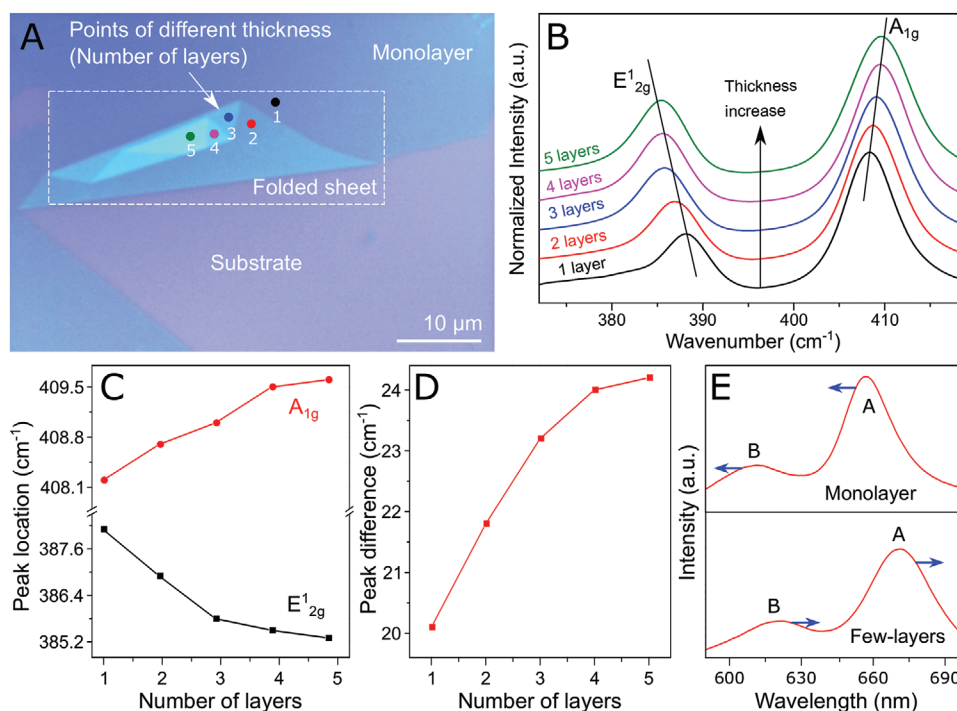
**ADVANCED
SCIENCE NEWS**

www.advancedsciencenews.com

**ADVANCED
FUNCTIONAL
MATERIALS**

www.afm-journal.de

Figure 4. Raman spectroscopy and PL characterizations of the 2D-MoS$_2$: A) Optical microscopy image of the 2D MoS$_2$. B) Raman spectra of 2D MoS$_2$ of different numbers of layers. C) A_{1g} and E^1_{2g} peak locations at different numbers of layers. D) The difference between peak locations of the A_{1g} and E^1_{2g} peaks for different numbers of layers. E) PL spectra of monolayer and bilayer 2D MoS$_2$.
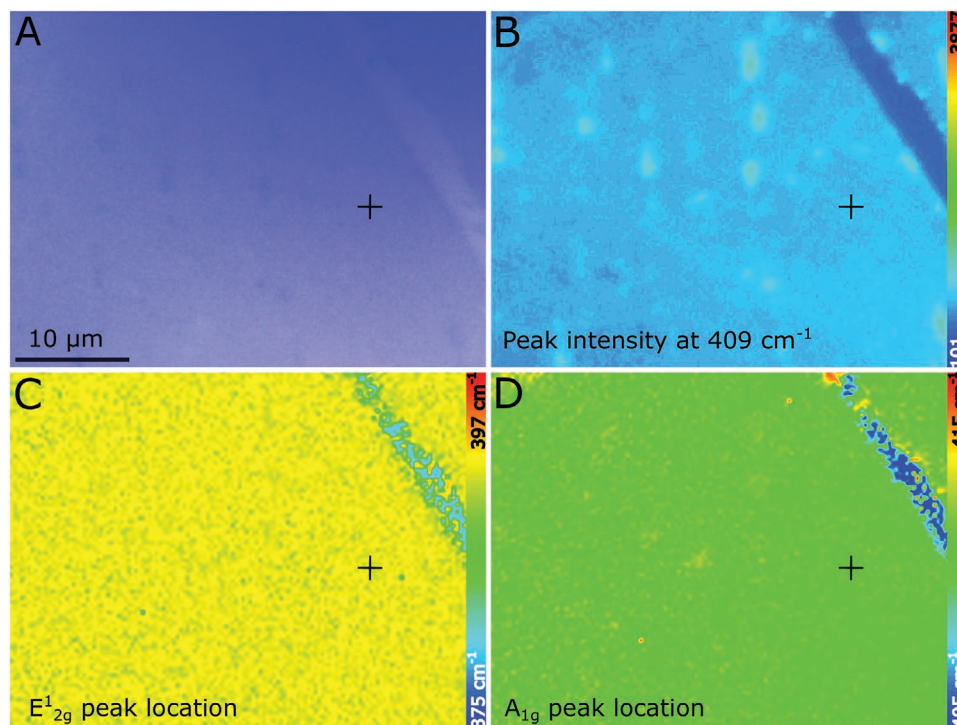

Figure 5. Raman mapping of a 2H-MoS$_2$ sheet. A single-point spectrum was collected at the point marked by a cross and shown in the Supporting Information. A) Optical microscopy image of the mapped region. B) Intensity mapping at 409 cm^{-1}. C) E^1_{2g} peak location mapping. D) A_{1g} peak location mapping.

image of a sample mapping region is shown in Figure 5A with the spatial distribution of the Raman peak intensities of this image depicted in Figure 5B. As can be seen in Figure 5B, the spatial map of peak intensity at 409 cm^{-1} (the approximate location of the A_{1g} peak) matches perfectly with the optical microscopy image contrast of the MoS_2 sheet. The majority of the 2D sheet shows a similar distribution of intensity, which indicts a high uniformity of the MoS_2 over a large area.

The spatial maps of the peak location of the E^1_{2g} and A_{1g} modes are presented in Figure 5C,D, respectively, for which single point spectra collected from the marked points are presented in Figure S12, Supporting Information, as an example. The peak locations difference of the E^1_{2g} and A_{1g} modes is approximately 20 cm^{-1}, which indicates monolayer MoS_2 over this area. The Raman mapping, with homogeneous color distribution on the images and relatively invariant peak intensities, further demonstrates the quality and uniformity of the large area 2H-MoS_2 monolayers that can be obtained using the developed liquid metal-based method.

3. Conclusions

In conclusion, we have demonstrated the possibility of forming 2D molybdenum sulfide on the surface of EGaIn. The EGaIn interface acted as a reactive and templating media simultaneously. The precursor, $(NH_4)_2MoS_4$, could be intrinsically destabilized and reduced on the surface of EGaIn at room temperature to establish interfacial molybdenum sulfide. With a series of electrochemical characterizations, we defined the surface reactions that constitute the formation of the interfacial 2D molybdenum compound. The layer could be readily exfoliated and transferred onto a desired substrate using a piezo stage of nm resolution. The annealing steps are included to complete the process for obtaining planar 2H-MoS_2 of different thicknesses. This current technique presents a universal procedure for the deposition of any 2D transition metal dichalcogenide (2D TMD) of large spatial dimensions that can be adapted for large-scale production purposes, rivalling conventional deposition and exfoliation methods for 2D TMDs. In addition, the autogenous potential detected on the liquid metal's surface can be controlled and harnessed for various chemical reactions.

4. Experimental Section

Materials: All the chemicals were used as received without further purification. Gallium (round shots, 99.9%) and indium (beads, 99.9%) were purchased from Rotometals, USA. Ammonium tetrathiomolybdate ($(NH_4)_2MoS_4$, 99.97%) was purchased from Sigma-Aldrich. Sodium hydroxide (NaOH, AR) pellets were obtained from Chem-Supply Pty Ltd. Hydrochloric acid (HCl, 32%) was purchased from Chem-Supply Pty Ltd. Potassium chloride (KCl, AR) was purchased from Chem-Supply Pty Ltd. Gold wire (0.25 mm in diameter, 99.99%) was purchased from Sigma-Aldrich. Milli-Q water (18.2 MΩ·cm at 25 °C) was used in all experiments.

Materials Preparation: Eutectic gallium indium alloy (EGaIn) was prepared in-house in order to avoid any unknown additives of commercial EGaIn. Gallium (75.5 wt%) and indium (24.5 wt%) metal mixture were melted at 180 °C on a hot plate. This temperature was well above the melting point of indium (156.5 °C). Upon melting, the liquid

alloy was stirred with a glass rod to ensure homogeneous fusion and then allowed to cool down at room temperature. The EGaIn alloy was transferred from/into the glass vial using a glass Pasteur pipette.

Self-Deposition of Molybdenum Sulfides (MoS_x) on Eutectic Alloy of Gallium and Indium: For the liquid metal-assisted synthesis of MoS_x, an EGaIn liquid droplet (120 μL) was placed in a plastic Petri dish (35 mm inner diameter, 36 mm outer diameter and 15 mm height). The surface of the EGaIn liquid was cleaned from the passive oxide layer by adding 5.0 mL of 5.0 M HCl directly onto the liquid metal droplet. The HCl instantly removed the oxide layer and the liquid metal droplet turned from a dull and deformed shape into a spherical and shiny ball. The HCl washing liquid was then removed and replaced with 5.0 mL of a 1.92 mM $(NH_4)_2MoS_4$ aqueous solution. The MoS_x interfacial layer formed immediately on the EGaIn droplet and the $(NH_4)_2MoS_4$ solution was diluted with 35 mL of Milli-Q water to halt the deposition process. The Petri dish was placed in a larger container so that the overflow from the dilution step could be contained. The solution in the vicinity of the MoS_x-bearing EGaIn droplet was gently removed and replaced with 5.0 mL of Milli-Q water. This was repeated another two times to ensure the cleanliness of the MoS_x-bearing EGaIn droplet. To ensure a successful transfer of the uniform and large interfacial layer, extra care was taken while washing the EGaIn droplet as any disturbance of the droplet could introduce microtears into the interfacial layer. Afterward, the MoS_x-bearing droplet was left to dry naturally at room temperature under an N_2 inert atmosphere.

Extraction and Transfer of MoS_x: The interfacial MoS_x was extracted from the surface of the EGaIn droplet and transferred to pre-cleaned substrates using a piezo-electric nano-positioning device (N-765 NEXACT precision z stage, 0.5 nm resolution, 25 N push/pull force, Physik Instrumente (PI) GmbH & Co. KG). Various substrates (Si, Si/SiO$_2$ (285 nm) and sapphire substrates) were utilized. The substrates were sonicated in acetone, isopropanol, and Milli-Q water for 10 min each and stored in isopropanol. Prior to use, the substrates were rinsed in Milli-Q water, blow-dried with nitrogen gas, and further cleaned with a Tergeo plasma cleaner-Pie Scientific, USA (15 W, 2.0 min). The pre-cleaned substrate (1.0 cm × 1.0 cm) was fixed upside-down on a holder (2.0 cm above the stage), and the MoS_x-bearing EGaIn droplet in the Petri dish was placed on the piezoelectric stage under the substrate. The piezo-electric stage then lifted the droplet towards the substrate with a speed of 0.20 mm s^{-1} until they were in contact. The contact was held for 5.0 s before the stage was brought down at the same speed, leaving the MoS_x layer behind on the substrate. Due to the van der Waals forces between the MoS_x layer and the solid substrate, the transferred MoS_x layer adhered strongly to the substrate. After the transfer, the substrate was removed from the holder and washed using an ultrasonic bath in ethanol to eliminate any residual liquid metal. To achieve a successful transfer, it was essential to completely dry the surfaces of the liquid metal droplet and the substrate. The wafer, carrying the transferred 2D materials, was immersed in 50 mM NaOH for 30 s, to wash away any oxidized gallium residues, rinsed with Milli-Q water and blow-dried with nitrogen gas.

Annealing Process: A three-step annealing process was adapted to further crystallize and sulfurize the resultant material into 2H-MoS_2. A tube furnace (Thermo Scientific, TF55030C-1) with a quartz tube (22 mm inner diameter, 25 mm outer diameter, and 1.0 m length) was utilized for annealing. In step one, the sample was annealed in a 5% H_2 (balanced in N_2) atmosphere at 500 °C for 60 min for initial crystallization. In step two, the sample was annealed in a 5% H_2 (balanced in N_2) and sulfur vapor at 750 °C for 20 min. In step three, the sample was annealed in ultra-pure argon and sulfur vapor at 850 °C for 20 min to further improve the quality of the 2D-MoS_2.

Electrochemical Analysis: All the electrochemical processes were carried out using an electrochemical workstation (CHI650E, CH Instruments Inc., USA). The reference cyclic voltammetry was performed in a standard three-electrode cell, with a gold-coated Si wafer (1.0 cm × 4.0 cm) as the working electrode, a spiral gold wire as the counter electrode, and a SCE as the reference. A glass cell (25 mm inner diameter and 40 mm height) was used, and the electrolyte was

**ADVANCED
SCIENCE NEWS**

www.advancedsciencenews.com

**ADVANCED
FUNCTIONAL
MATERIALS**

www.afm-journal.de

an aqueous solution of 1.92 mM $(NH_4)_2MoS_4$ and 0.10 M KCl as the supporting electrolyte. Different scan rates (25, 50, and 100 mV s^{-1}) were used at a resolution of 1.0 mA V^{-1}, with a potential window from −1.3 V to 1.0 V.

The open-circuit voltage (V_{oc}) analysis of the EGaIn droplet was performed in a standard three-electrode system with EGaIn as the working electrode. A plastic Petri dish (35 mm inner diameter, 36 mm outer diameter, and 15 mm height) was used as the cell, 0.10 M KCl solution as the electrolyte, SCE as the reference, and a spiral gold wire as the counter electrode. An EGaIn droplet (120 μL) was used as the working electrode, and a gold wire (inside a glass tube) was connected to the droplet by immersing one end of it into the EGaIn droplet. The EGaIn electrode was washed with 5.0 mL of 5.0 M HCl which was then removed and replaced with 0.10 M KCl solution as the supporting electrolyte for the measurement. Prior to the measurement, the electrolyte was adjusted to the same pH as the $(NH_4)_2MoS_4$ precursor solution, monitored by a pH meter.

EIS was carried out in the same three-electrode system as the V_{oc} measurement, with 1.92 mM $(NH_4)_2MoS_4$ and 0.10 M KCl as the electrolyte. The frequency range was 1.0 Hz to 10^5 Hz, with −0.50 V used as the initial voltage with a 5.0 mV amplitude. For the EIS measurement of the EGaIn droplet without the self-deposited MoS$_x$ layer, 5.0 mL of 5.0 M HCl was used for cleaning the surface of the EGaIn droplet before the measurement. The remnant of the HCl liquid was then removed and replaced with the electrolyte. For the measurement of the MoS$_x$-bearing EGaIn droplet, MoS$_x$ was self-deposited onto an EGaIn electrode as described above, and then the EIS measurement was performed. In order to make the deposition layer intact during the measurement, a gold wire was connected to the droplet prior to the deposition.

Electrochemical Deposition of MoS$_x$: The electrochemical deposition of molybdenum sulfide was carried out by voltammetric runs (scan rate 50 mV s^{-1}, 10 cycles) using the same three-electrode cell as described in the electrochemical analysis section.

Morphological Characterization: AFM images were collected using a Bruker dimension icon SPM (USA) with a ScanAsyst-Air probe (Bruker AFM probes, USA). Each sample was scanned as prepared without further processing using the PeakForce Tapping mode. A scan rate of 0.50 Hz and a resolution of 250 samples line^{-1} was applied. A vacuum was utilized to stabilize the specimens on the AFM stage. R_a and depth distribution profiles were obtained with Nanoscope Analysis software.

High-resolution AFM images were obtained using a Cypher ES AFM (Oxford Instrument, Asylum Research, Santa Barbara, CA, USA) in ambient room temperature (25 °C) conditions using an amplitude modulated-AFM. ArrowUHF (NanoWorld, Switzerland, nominal spring constant k_c = 6 N m^{-1}) were used for all images. To minimize the imaging force, a setpoint ratio (Imaging Amplitude (A)/free amplitude (A_0)) of > 0.8 was maintained during imaging (unless otherwise stated). Cantilevers were calibrated using the thermal spectrum method, in air, prior to use, and the lever sensitivity was determined using force spectroscopy; the spring constant was resolved via the inverse optical lever sensitivity (InVOLS) using force curve measurements on the hard surface.

SEM (JEOL JSM-IT 500 HR) coupled with energy-dispersive X-ray spectroscopy (EDS, Bruker Silicon) was used for morphological and elemental analyses of the electro-deposited materials.

A Philips CM200 field-emission HR-TEM system equipped with a GATAN ORIUS camera was employed for atomic-resolution morphological and lattice structure analysis. A thermally robust silicon nitride (Si$_3$N$_4$) grid (Ted Pella, 2 158 710) was employed for the TEM sample.

Optical Characterization: XPS analysis was carried out using a Thermo Scientific ESCALAB250i high-resolution XPS (UK) with monochromatic Al Kalpha soft X-ray source (1486.68 eV), 2×10^{-9} mbar background vacuum, 90° photoelectron take-off angle, 120 W power (13.8 kV × 8.7 mA), and 500 μm spot size. For calibration, C1s = 284.8 eV for adventitious hydrocarbon was used as a reference. Avantage XPS software (from Avantage Software Ltd, United Kingdom) was used for fitting and deconvoluting the high-resolution XPS spectra.

A Renishaw inVia Raman microspectrometer (Gloucestershire, UK) equipped with 532 nm laser and WiRE was utilized for Raman spectra collection. One second exposure time, 200 accumulations with 1% laser power and 100 times magnification were used for single-point spectral acquisition. Raman mapping was obtained by raster scanning at 100 times magnification with a step-size of 0.3 μm, where a spectrum at each point was collected with 5% laser power, 1 s exposure time, and one accumulation.

Supporting Information

Supporting Information is available from the Wiley Online Library or from the author.

Acknowledgements

Conflict of Interest

The authors declare no conflict of interest.

Keywords

[1] H. Okamoto, T. B. Massalski, *Binary Alloy Phase Diagrams*, ASM International, Materials Park, Ohio **1990**.

[2] a) T. Daeneke, K. Khoshmanesh, N. Mahmood, I. A. de Castro, D. Esrafilzadeh, S. Barrow, M. Dickey, K. Kalantar-Zadeh, *Chem. Soc. Rev.* **2018**, *47*, 4073; b) K. Kalantar-Zadeh, J. B. Tang, T. Daeneke, A. P. O'Mullane, L. A. Stewart, J. Liu, C. Majidi, R. S. Ruoff, P. S. Weiss, M. D. Dickey, *ACS Nano* **2019**, *13*, 7388; c) X. Sun, B. Yuan, L. Sheng, W. Rao, J. Liu, *Appl. Mater. Today* **2020**, *20*, 100722; d) S.-Y. Tang, D. R. Mitchell, Q. Zhao, D. Yuan, G. Yun, Y. Zhang, R. Qiao, Y. Lin, M. D. Dickey, W. Li, *Matter* **2019**, *1*, 192; e) H. Z. Wang, Y. Y. Yao, Z. Z. He, W. Rao, L. Hu, S. Chen, J. Lin, J. Y. Gao, P. J. Zhang, X. Y. Sun, X. Wang, Y. Cui, Q. Wang, S. Dong, G. Chen, J. Liu, *Adv. Mater.* **2019**, *31*, 1901337.

[3] C. S. Ivanoff, A. E. Ivanoff, T. L. Hottel, *Food Chem. Toxicol.* **2012**, *50*, 212.

[4] a) B. J. Carey, J. Z. Ou, R. M. Clark, K. J. Berean, A. Zavabeti, A. S. Chesman, S. P. Russo, D. W. Lau, Z. Q. Xu, Q. Bao, O. Kavehei, B. C. Gibson, M. D. Dickey, R. B. Kaner, T. Daeneke, K. Kalantar-Zadeh, *Nat. Commun.* **2017**, *8*, 14482; b) N. Syed, A. Zavabeti, K. A. Messalea, E. D. Gaspera, A. Elbourne, A. Jannat, M. Mohiuddin, B. Y. Zhang, G. Zheng, L. Wang, S. P. Russo, D. Esrafilzadeh, C. F. McConville, K. Kalantar-Zadeh, T. Daeneke, *J. Am. Chem. Soc.* **2019**, *141*, 104; c) C. Li, M. Iqbal, J. Lin, X. Luo, B. Jiang, V. Malgras, K. C.-W. Wu, J. Kim, Y. Yamauchi, *Acc. Chem. Res.* **2018**, *51*, 1764; d) C. Li, M. Iqbal, B. Jiang, Z. Wang, J. Kim, A. K. Nanjundan, A. E. Whitten, K. Wood, Y. Yamauchi, *Chem. Sci.*

2019, *10*, 4054; e) B. Jiang, Y. Guo, J. Kim, A. E. Whitten, K. Wood, K. Kani, A. E. Rowan, J. Henzie, Y. Yamauchi, *J. Am. Chem. Soc.* **2018**, *140*, 12434; f) C. Li, H. Tan, J. Lin, X. Luo, S. Wang, J. You, Y.-M. Kang, Y. Bando, Y. Yamauchi, J. Kim, *Nano Today* **2018**, *21*, 91.

[5] H. Khan, N. Mahmood, A. Zavabeti, A. Elbourne, M. A. Rahman, B. Y. Zhang, V. Krishnamurthi, P. Atkin, M. B. Ghasieman, J. Yang, G. Zheng, A. R. Ravindran, S. Walia, L. Wang, S. P. Russo, T. Daeneke, Y. X. Li, K. Kalantar-Zadeh, *Nat. Commun.* **2020**, *11*, 3449.

[6] M. Mayyas, H. Li, P. Kumar, M. B. Ghasemian, J. Yang, Y. Wang, D. J. Lawes, J. Han, M. G. Saborio, J. Tang, R. Jalili, S. H. Lee, W. K. Seong, S. P. Russo, D. Esrafilzadeh, T. Daeneke, R. B. Kaner, R. S. Ruoff, K. Kalantar-Zadeh, *Adv. Mater.* **2020**, *32*, 2001997.

[7] a) Q. H. Wang, K. Kalantar-Zadeh, A. Kis, J. N. Coleman, M. S. Strano, *Nat. Nanotechnol.* **2012**, *7*, 699; b) S.-S. Chee, J.-H. Lee, K. Lee, M.-H. Ham, *ACS Appl. Mater. Interfaces* **2019**, *12*, 4129; c) S. S. Chee, W. J. Lee, Y. R. Jo, M. K. Cho, D. Chun, H. Baik, B. J. Kim, M. H. Yoon, K. Lee, M. H. Ham, *Adv. Funct. Mater.* **2020**, *30*, 1908147; d) D. S. Fox, Y. Zhou, P. Maguire, A. O'Neill, C. Ó'Coileáin, R. Gatensby, A. M. Glushenkov, T. Tao, G. S. Duesberg, I. V. Shvets, M. Abid, M. Abid, H.-C. Wu, Y. Chen, J. N. Coleman, J. F. Donegan, H. Zhang, *Nano Lett.* **2015**, *15*, 5307; e) C. Iffelsberger, S. Ng, M. Pumera, *Appl. Mater. Today* **2020**, *20*, 100654; f) Y. Liu, X. He, D. Hanlon, A. Harvey, J. N. Coleman, Y. Li, *ACS Nano* **2016**, *10*, 8821; g) S. Manzeli, D. Dumcenco, G. M. Marega, A. Kis, *Nat. Commun.* **2019**, *10*, 4831; h) M. Negri, L. Francaviglia, D. Dumcenco, M. Bosi, D. Kaplan, V. Swaminathan, G. Salviati, A. Kis, F. Fabbri, A. F. i Morral, *Nano Lett.* **2020**, *20*, 567; i) A. R. Rezk, B. Carey, A. F. Chrimes, D. W. Lau, B. C. Gibson, C. Zheng, M. S. Fuhrer, L. Y. Yeo, K. Kalantar-zadeh, *Nano Lett.* **2016**, *16*, 849; j) V. Urbanová, P. Lazar, N. Antonatos, Z. k. Sofer, M. Otyepka, M. Pumera, *ACS Appl. Mater. Interfaces* **2020**, *12*, 20383; k) Y. Wang, J. Z. Ou, A. F. Chrimes, B. J. Carey, T. Daeneke, M. M. Alsaif, M. Mortazavi, S. Zhuiykov, N. Medhekar, M. Bhaskaran, J. R. Friend, M. S. Strano, K. Kalantar-Zadeh, *Nano Lett.* **2015**, *15*, 883.

[8] D. Landolt, *Corrosion and Surface Chemistry of Metals*, CRC press, Boca Raton, Florida **2007**.

[9] W. Schmickler, R. Guidelli, *Electrochim. Acta* **2014**, *127*, 489.

[10] H. Helmoltz, *Ann. Phys. Chem.* **1853**, *3*, 353.

[11] E. Quagraine, I. Georgakaki, D. Coucouvanis, *J. Inorg. Biochem.* **2009**, *103*, 143.

[12] a) E. Ponomarev, M. Neumann-Spallart, G. Hodes, C. Lévy-Clément, *Thin Solid Films* **1996**, *280*, 86; b) D. Belanger, G. Laperriére, B. Marsan, *J. Electroanal. Chem.* **1993**, *347*, 165.

[13] a) M. B. Ghasemian, M. Mayyas, S. A. Idrus-Saidi, M. A. Jamal, J. Yang, S. S. Mofarah, E. Adabifiroozjaei, J. Tang, N. Syed, A. P. O'Mullane, T. Daeneke, K. Kalantar-Zadeh, *Adv. Funct. Mater.* **2019**, *29*, 1901649; b) J. Lyu, M. Mayyas, O. Salim, H. Zhu, D. Chu, R. Joshi, *Mater. Today Energy* **2019**, *13*, 277.

[14] F. W. DelRio, M. P. de Boer, J. A. Knapp, E. D. Reedy, P. J. Clews, M. L. Dunn, *Nat. Mater.* **2005**, *4*, 629.

[15] Z. Liu, X. Zhang, B. Wang, M. Xia, S. Gao, X. Liu, A. Zavabeti, J. Z. Ou, K. Kalantar-Zadeh, Y. Wang, *J. Phys. Chem. C* **2018**, *122*, 12589.

[16] Y. H. Lee, X. Q. Zhang, W. Zhang, M. T. Chang, C. T. Lin, K. D. Chang, Y. C. Yu, J. T. W. Wang, C. S. Chang, L. J. Li, T.-W. Lin, *Adv. Mater.* **2012**, *24*, 2320.

[17] a) S. Ghatak, A. N. Pal, A. Ghosh, *ACS Nano* **2011**, *5*, 7707; b) B. Radisavljevic, A. Radenovic, J. Brivio, V. Giacometti, A. Kis, *Nat. Nanotechnol.* **2011**, *6*, 147.

[18] H. Li, Q. Zhang, C. C. R. Yap, B. K. Tay, T. H. T. Edwin, A. Olivier, D. Baillargeat, *Adv. Funct. Mater.* **2012**, *22*, 1385.

[19] a) H. Liu, D. Chi, *Sci. Rep.* **2015**, *5*, 11756; b) J. Jeon, S. K. Jang, S. M. Jeon, G. Yoo, Y. H. Jang, J.-H. Park, S. Lee, *Nanoscale* **2015**, *7*, 1688; c) S. Najmaei, Z. Liu, W. Zhou, X. Zou, G. Shi, S. Lei, B. I. Yakobson, J.-C. Idrobo, P. M. Ajayan, J. Lou, *Nat. Mater.* **2013**, *12*, 754.

[20] G. Eda, H. Yamaguchi, D. Voiry, T. Fujita, M. Chen, M. Chhowalla, *Nano Lett.* **2011**, *11*, 5111.

[21] K. P. Dhakal, D. L. Duong, J. Lee, H. Nam, M. Kim, M. Kan, Y. H. Lee, J. Kim, *Nanoscale* **2014**, *6*, 13028.